Multifunctional and sustainable vitrimer systems for self-healing, scratch resistance, and corrosion protection

Advanced Optical Materials

ADVANCED OPTICAL MATERIALS
www.advopticalmat.de

RESEARCH ARTICLE OPEN ACCESS

Temperature-Dependent Properties of Amino-As Based InAs/ZnSe Core-Shell Quantum Dot Films

Mukesh Kumar Thakur[1,6] | Guncem Ozgun Eren[1] | Meenakshi Pegu[2] | Houman Bahmani Jalali[1] | Magdhi Kirti[1] | Matteo Lorenzoni[3] | Mirko Prato[3] | Yurii P. Ivanov[4] | Giorgio Divitini[4] | Ilka Kriegel[5] | Liberato Manna[2] | Francesco Di Stasio[1]

[1]Photonic Nanomaterials, Istituto Italiano di Tecnologia, Genova, Italy | [2]Nanochemistry, Istituto Italiano di Tecnologia, Genova, Italy | [3]Materials Characterization Facility, Istituto Italiano di Tecnologia, Genova, Italy | [4]Electron Spectroscopy and Nanoscopy, Istituto Italiano di Tecnologia, Genova, Italy | [5]Dipartimento Di Scienza Applicata e Tecnologie (DISAT), Politecnico di Torino, Torino, Italy | [6]Department of Applied Physics, Indian Institute of Information Technology Vadodara - ICD, India

Correspondence: Francesco Di Stasio (francesco.distasio@iit.it)

Received: 16 September 2025 | **Revised:** 30 January 2026 | **Accepted:** 3 February 2026

Keywords: conductivity | InAs/ZnSe core-shell | quantum dots | thermal stability | work function

ABSTRACT

Restriction of Hazardous Substances (RoHS) compliant InAs colloidal quantum dots (CQDs) are a class of promising nanomaterials for near infrared optoelectronics. However, the presence of long-chain organic ligands severely limits their electrical conductivity, and the influence of temperature on ligand dynamics remains poorly understood. Here, we investigate spin-coated InAs/ZnSe CQD thin films on SiO_2/Si substrates subjected to annealing up to 300°C in air. Steady-state and time-resolved photoluminescence measurements reveal that emission properties are partially preserved up to 250°C. Raman spectroscopy and X-ray diffraction (XRD) analyses confirm the retention of crystal structure throughout the annealing process. Notably, Kelvin probe force microscopy (KPFM) indicates a substantial change in contact potential difference (CDP) at 250°C, coinciding with a pronounced increase in electrical conductivity from current density-voltage measurements. This enhancement is attributed to the partial desorption of oleylamine (OLA) ligands, as supported by Raman, Fourier transform infrared spectroscopy (FTIR), Thermogravimetric analysis (TGA) and X-ray Photoelectron Spectroscopy (XPS) analyses, which lowers interparticle barriers and facilitates charge transport while maintaining film morphology. These findings highlight the critical interplay between ligand chemistry, structural stability, and charge transport, demonstrating that thermal annealing provides an effective pathway to enhance electrical performance while preserving optical quality in InAs/ZnSe CQD films.

1 | Introduction

Colloidal quantum dots (CQDs) have emerged as a promising class of nanomaterials due to their exceptional optical, electronic, and chemical properties coupled with the capability for large-scale production [1–4]. This scalability opens unique opportunities to harness CQDs for diverse applications, including high-temperature sensors [5, 6]. The size and composition of CQDs can be precisely tuned, enabling manipulation of their optoelectronic properties, rendering CQDs suitable for a broad spectrum of uses [2, 3, 7, 8]. In medicine, they are extensively employed in bio-imaging and diagnostics applications owing to their strong and stable fluorescence [9–11]. In electronics, CQDs hold potential for the fabrication of photodetectors, light-emitting diodes (LEDs), and solar cells, also owing to their solution-processable nature, which facilitates low-cost, large-area film preparation, providing an advantage over traditional semiconductor materials [5, 12–18]. Substantial progress has been achieved in UV–Vis light-emitting

CQDs for commercial applications as an environmentally friendly technology, given that some CQDs can be synthesized via green chemistry approaches (e.g., graphene CQDs have been produced using leaves of the date palm tree) [19, 20]. In contrast, CQDs widely used in near-infrared (NIR) applications such as photodetectors, LEDs and cameras are mostly based on mercury (Hg)- or lead (Pb)-chalcogenides [21–23]. However, compliance with the Restriction of Hazardous Substances (RoHS) directive requires the development of less toxic alternative materials [24]. In this context, indium arsenide (InAs) CQDs have recently emerged as key nanomaterials for NIR technologies due to their RoHS compliance and tunable absorption spanning from 850 nm to beyond 2000 nm. [17, 24–28] Furthermore, employing ZnSe as a shell material on an InAs core significantly enhances the photoluminescence quantum yield (PLQY), making them ideal candidates for NIR light-sources [24, 25, 29, 30]. In recent years, several studies, including our own, have explored the potential of InAs/ZnSe CQDs [31–33]. For instance, our group has successfully demonstrated NIR LEDs operating > 900 nm, utilizing InAs/ZnSe CQDs as active material [23, 24]. Similarly, Sheikh et al. [34, 35] have reported a NIR photodetector based on InAs/ZnSe nanorods [36]. Another noteworthy contribution comes from the Jeong group, who demonstrated the first p–n junction solar cell using both n-type and p-type InAs CQDs as the primary light-harvesting materials, achieving a power conversion efficiency of approximately 2% under one sun illumination [37]. These examples highlight the versatility of InAs CQDs for NIR applications [38]. However, one of the major challenges limiting the standalone application of InAs/ZnSe CQDs is the presence of long-chain organic ligands, such as oleylamine (OLA), that hinder electrical transport in their respective solids [17, 18, 36].

Recent ligand-exchange, doping and surface treatment methods have been demonstrated to improve CQD coupling and carrier mobility [39–43]. For example, replacing OLA with indium (III) bromide ($InBr_3$) reduces ligand length and enhances film conductivity [35, 44]. However, OLA ligands are temperature-sensitive, and their decomposition upon annealing can also boost electrical conductivity [45]. Yet, to the best of our knowledge, there have been no comprehensive report focusing solely on the intrinsic electrical properties and thermal stability of films based on pristine InAs cores or InAs/ZnSe CQDs.

In this work, we systematically investigated the optical, structural, and electrical properties of InAs/ZnSe CQD thin films prepared via spin-coating onto SiO_2/Si and glass substrates. The films were annealed in ambient air from room temperature (RT) up to 300 °C. Our results reveal that annealing at 200 °C and 250 °C preserves the structural integrity of the CQDs, as confirmed by photoluminescence (PL), Raman spectroscopy, X-ray diffraction (XRD), and X-ray photoelectron spectroscopy (XPS). Nonetheless, at 300°C, we observe degradation of the CQD film, with the formation of oxides. Notably, Kelvin probe force microscopy (KPFM) shows a significant increment in contact potential difference (CPD) with increasing annealing temperature. At 250 °C, the films exhibit the onset of electrical conductivity, forming a Schottky junction while retaining PL and structural integrity. The improved conduction is attributed to the removal or decomposition of OLA ligands, as further evidenced by Raman spectroscopy, Fourier-transform infrared spectroscopy (FTIR) and XPS analyses. Our work demonstrates a straightforward processing of InAs/ZnSe CQD films for diverse applications and provides a fundamental study of their thermal and electrical properties.

2 | Results and Discussion

The InAs/ZnSe CQDs were synthesized following a previously reported method [29]. Briefly, InAs core CQDs were prepared by using zinc chloride ($ZnCl_2$) as an additive, tris(dimethylamino) arsine (amino-As) as the arsenic precursor, and alane *N, N*-dimethylethylamine complex (DMEA-AlH_3, 0.5 M solution in toluene) as reducing agent. The reaction was carried out at 300°C for 15 min, after which it was quenched to 90°C. Then, a ZnSe shell was grown in situ by injecting zinc chloride-OLA ($ZnCl_2$-OLA, 0.8 M) and tri-n-octylphosphine-selenium (TOP-Se, 1 M) precursors at 90°C, followed by heating the system to 310°C for an additional 2 h [25, 29]. The details about the synthesis are given in the Experimental Section.

An optical image together with optical absorption (Abs) and PL spectra of the as-synthesized InAs/ZnSe CQD solution are shown in the Supporting Information (Figure S1a,b). The InAs/ZnSe CQDs exhibit a broad Abs profile, with a prominent excitonic peak around 850 nm. Correspondingly, the PL spectrum shows a peak centered near 900 nm, in agreement with our previous reports [17, 25]. The low-resolution transmission electron microscopy (TEM) analysis (Figure S1c,d) reveals that the CQDs are uniformly dispersed with an average size of ≈11 nm. Atomic resolution High-Angle Annular Dark Field Scanning TEM (HAADF-STEM) images, in combination with Energy Dispersive X-ray elemental analysis (STEM-EDX), confirmed the tetrahedral shape and the composition of the resulting core/shell CQDs [29] (see Figures S2 and S3).

The InAs/ZnSe CQD solutions were then used to fabricate thin films via spin-coating (Figure). The CQD solution was deposited onto clean substrates and spun at 2000 rpm for 1 min to achieve uniform film coverage and a film thickness of ~180 nm (Figure S5a,b). Films were then annealed at different temperatures (200°C, 250°C and 300°C) for 20 min, then let cool down to RT to be used in the various analyses. The surface morphology and roughness of the InAs/ZnSe CQD thin films were analyzed using high-resolution scanning electron microscopy (HR-SEM), and atomic force microscopy (AFM) as shown in Figures 1a,b. At room temperature (RT), the film exhibits a root mean square (RMS) roughness (calculated from AFM images) of 2.8 ± 0.2 nm, suggesting a relatively high surface homogeneity (Figure 1a).

Upon annealing at 200°C, AFM topography reveals that the RMS roughness slightly increases to 3.0 ± 0.3 nm (Figure S6a). This indicates partial CQDs rearrangement as surface OLA ligands might begin to desorb, allowing particles to pack more closely, while maintaining overall film uniformity. At 250°C, (Figure S6b) the RMS roughness increases to 3.5 ± 0.3 nm, likely due to ligand desorption (this will be discussed later in the work). At 300°C, the film shows a decrease in RMS roughness to approximately 2.5 ± 0.2 nm (Figure S6c); yet an irregular and porous morphology can be observed [46, 47]. The emergence of pores likely results from excessive ligand removal and thermal stress during annealing [48] (the RMS values are provided in Table S1). Scanning electron

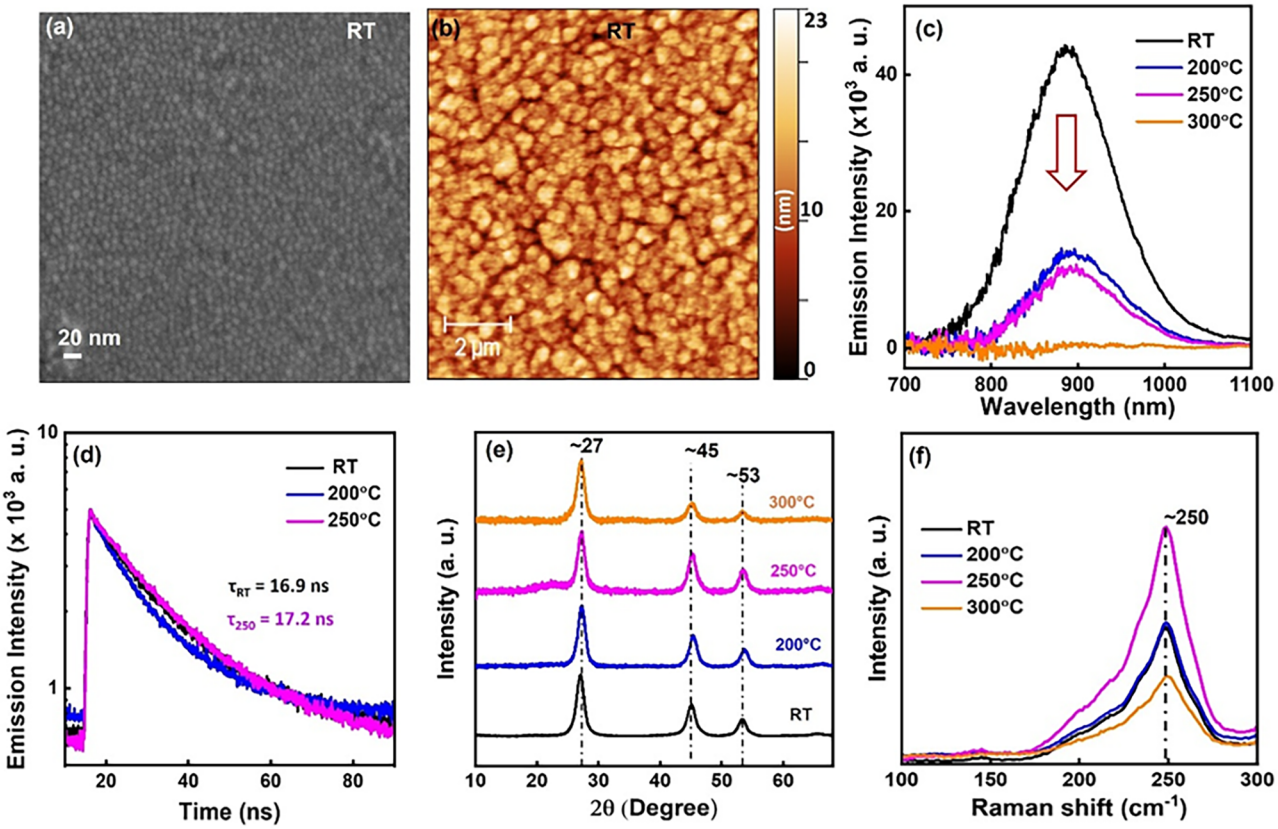

FIGURE 1 | (a) SEM and (b) AFM images of an InAs/ZnSe CQD film at RT. (c) PL spectra of the InAs/ZnSe CQD films at different annealing temperatures showing emissions up to 250°C. At 300°C, the PL vanishes, indicating CQDs degradation. (d) Time-resolved photoluminescence (TRPL) curves measured at RT, 200 °C, and 250°C, evidence partially preserved radiative recombination dynamics upon annealing. (e) X-ray diffraction (XRD) patterns of the films annealed at increasing temperatures up to 300 °C, displaying sharp diffraction peaks around 27°, 45°, and 53°, consistent with the preserved crystalline structure of CQDs. (f) Raman spectra collected at increasing annealing temperatures featuring a dominant phonon mode at ~250 cm^{-1}, characteristic of ZnSe. The minimal shift and broadening with temperature confirm the structural robustness of the InAs/ZnSe CQDs under thermal stress.

microscopy (SEM) images corroborate the observation from the AFM analysis, with a lack of significant changes up to 250°C (Figure S6d–f). At 300°C (Figure S6f), although the film remains continuous, a noticeable reduction in contrast is observed. This change can be tentatively assigned to alterations in surface chemistry, such as ligand decomposition or loss [45, 49].

The low-magnification SEM images along with the corresponding elemental analysis are presented in Figures S7–S10, clearly demonstrating that the major components (In, As, Zn, and Se) are uniformly distributed across the film also upon annealing.

The temperature-dependent PL spectra of InAs/ZnSe CQD thin films are shown in Figure 1c. The PL spectrum measured at RT exhibits a peak centered around ~900 nm, consistent with previous findings [17, 24]. After annealing, the PL shows ≈ 70% and ≈ 75% drop in intensity at 200°C, and 250 °C, respectively (Table S2). The full-width-at-half-maximum (FWHM, Figure S11a) remains nearly identical through the annealing process (from 122 nm for RT to 118 nm for 250°C). At 300 °C, no clear PL signal can be observed; however, micro-PL measurements reveal that the InAs/ZnSe CQD film still emits in the NIR region, although with very low intensity, indicating degradation (Figure S11b). Furthermore, we have studied the optical and structural properties using time-resolved photoluminescence (TRPL), XRD, and Raman spectroscopy (Figure 1d–f). The PL decay profiles (Figure 1d) exhibit average lifetime of approximately 16.9 ns at RT and 17.2 ns after annealing at 250 °C. Importantly, after annealing at 250°C, the TRPL presents a single-exponential decay, while at lower temperatures, a bi-exponential function was required to fit the time trace. Such variation in dynamics indicates major modifications in the exciton recombination pathways which are accompanied by a drop in PL intensity and induced by degradation of the material [50] (the details about the lifetime fitting are provided in Figures S12, and Table S3). XRD patterns of the InAs/ZnSe CQD films (Figure 1e) present clear peaks at ~27°, 45°, and 53°, which remain unchanged across all annealing temperatures [25]. The lack of modification upon annealing (e.g., broadening or shifts) indicates that the crystalline structure of the CQDs is preserved, without any phase transformation [48]. In particular, the persistent ZnSe- peak at ~27° suggests that the ZnSe shell remains intact even at higher temperatures [51]. The Raman spectra of InAs core CQDs (Figure S13) and InAs/ZnSe CQDs (Figure 1f) were recorded under 514 nm excitation (the experimental details are provided in the Experimental Section). The InAs core CQDs display a prominent Raman peak near 230 cm^{-1} (Figure S13), which arises from the longitudinal optical (LO) phonon mode characteristic of InAs core [52, 53]. Interestingly,

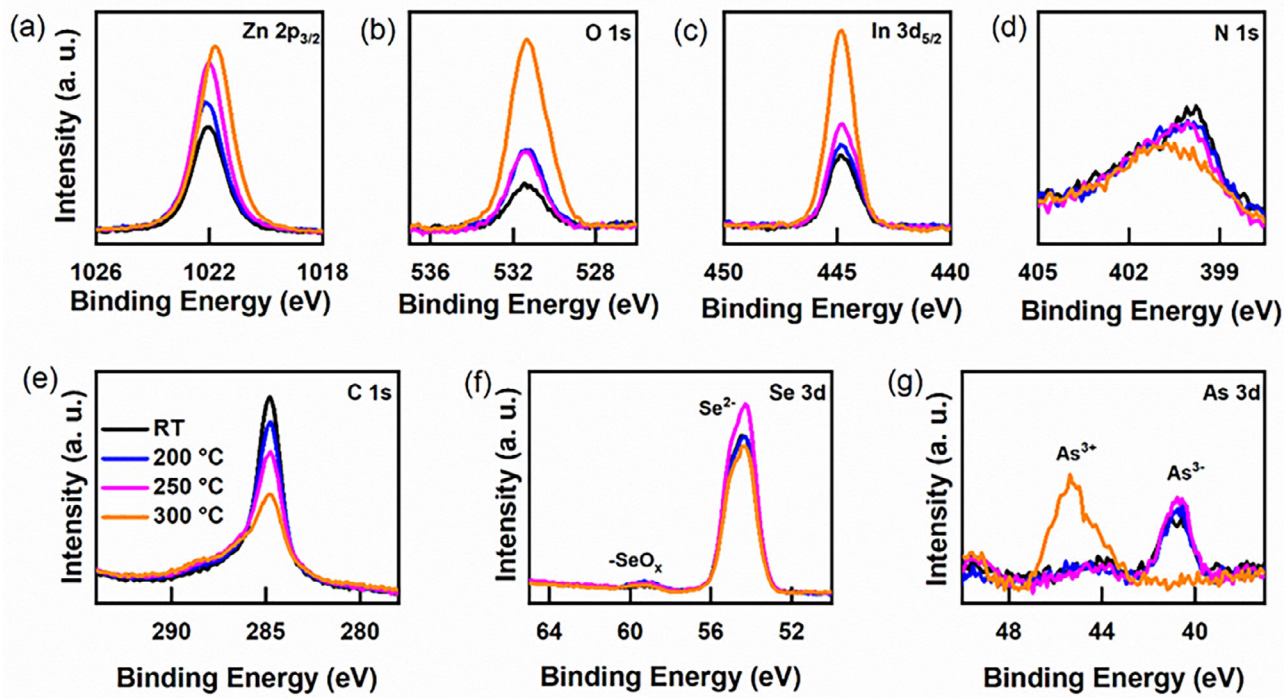

FIGURE 2 | Comparison of the XPS data collected on the InAs/ZnSe CQD films before (RT) and after thermal treatment at 200, 250, and 300°C. (a) Zn $2p_{3/2}$, (b) O 1s, (c) In $3d_{5/2}$, (d) N 1s, (e) C 1s, (f) Se 3d, (g) As 3d spectra.

upon formation of the ZnSe shell, the LO phonon peak broadens and shifts to a higher wavenumber, with spectra exhibiting a pronounced peak near 250 cm^{-1}, characteristics of ZnSe, attributed to the first-order LO phonon mode [54]. The peak shift serves as a direct indication of successful ZnSe shell formation and reflects the vibrational properties of the material [54–56]. This Raman feature (250 cm^{-1}) remains clearly visible across all annealing temperatures, indicating that the core-shell structure is preserved during the thermal treatment. Notably, the intensity of this peak increases significantly upon annealing at 250°C, suggesting an improved phonon coupling among adjacent CQDs, leading to a stronger Raman scattering [57–59]. However, annealing at 300°C leads to a strong decrease in Raman intensity. While variations in Raman peak intensity can arise from changes in film morphology or other experimental factors, the pronounced reduction observed here is primarily attributed to enhanced phonon-phonon scattering induced by the thermal treatment [42]. To further investigate these temperature-induced modifications, we performed Fourier transform infrared spectroscopy (FTIR) [18]. The FTIR spectra are reported in Figure S14 and they clearly exhibit the characteristic vibrational features of OLA ligands on the InAs CQD surface, including the C—H stretching modes near 2850–2920 cm^{-1} and the N—H bending vibrations in the 1580–1620 cm^{-1} region. A noticeable decrease in the intensity of these OLA-related peaks is observed as the annealing temperature increases from 200°C to 300°C. This progressive reduction indicates partial removal and thermal decomposition of the surface-bound OLA ligands, confirming effective ligand desorption upon heating [45]. To explore ligand desorption more deeply and quantify these changes, we performed XPS on all samples to investigate more quantitatively both the structural features and the elemental composition. The results obtained are shown in Figure 2a–g. The data collected at RT are in agreement with previous reports from our group on InAs/ZnSe core-shell system [25, 29]. In particular, the Zn $2p_{3/2}$ peak is centered at (1022.0 ± 0.2) eV; the In $3d_{5/2}$ peak is slightly asymmetrical, with a main component at (444.9 ± 0.2) eV due to the In-Zn-Se interlayer between core and shell, and a minor component at (444.1 ± 0.2) eV from the InAs core; the Se 3d main signal is centered at (54.2 ± 0.2) eV, in line with reports on ZnSe [60], and it is accompanied by a low intensity signal at approx. 59 eV, indicative of slight surface oxidation forming SeO_2 species (Figure 2f) [61]; the As 3d main signal is centered at (40.6 ± 0.2) eV, in line with previous reports [29]. Oxygen has also been detected on the surface of the film, due to exposure of the sample to air. It is relevant to highlight that the presence of carbon (C 1s peak at 284.8 eV) and nitrogen (N 1s peak at approx. 399.8 eV, originating from the $-NH_2$ group of OLA in the ligand shell) overlap with Se-related spectral features (see Figure S15).

The main effect of the thermal treatment up to 250°C is the gradual removal of the organic OLA ligands, as evidenced by the decrease in intensity of the C 1s peak, shown in Figure 2e. The nitrogen content gradually decreased as well, with the [N]/[Se] ratio going from 0.07 at RT to 0.02°C at 250°C. The partial removal of the organic ligands also impacted other XPS signals, which gained intensity due to the reduced effective thickness of the organic coating. Apart from this change, the thermal treatments did not affect the chemistry of the system, as all the spectral features discussed for the sample at RT are still visible up to 250°C. The situation changes after the annealing at 300°C: the C 1s intensity further decreases, and the nitrogen signal drops below sensitivity ([N]/[Se] = 0). The Zn signal increases in intensity and shifts to slightly lower binding energy, while the Se signal decreases in intensity while keeping the same spectral position (i.e., same oxidation state). The In $3d_{5/2}$ peak almost doubles in intensity and becomes more symmetrical in shape, and it is now

centered at (444.8 ± 0.2) eV. The oxygen signal greatly increases as well. The main observed effect is on the arsenic features: the original signal due to arsenide, centered at approx. 41 eV, disappears, and all the As of the system is in an oxidized form, as evidenced by the signal now centered at approx. 45 eV, indicative of the presence of As(III) and As(V) oxides [62]. The XPS investigation therefore suggests a quite relevant restructuring of the InAs/ZnSe system upon thermal treatment at 300°C, with the In and As species from the core being more exposed to the environment (either due to migration into the shell or to partial shell cracking) and subsequently being oxidized. It has also been reported that the annealing environment significantly affects CQDs [45]. To study this effect, we first performed PL measurements on InAs/ZnSe CQD films annealed under N_2 atmosphere and compared them with films annealed in air, as shown in Figure S16. A clear reduction in PL intensity is observed for the samples annealed in air compared to those in N_2, while the peak position remains unchanged, suggesting that oxidation, rather than intrinsic structural changes is primarily responsible for the quenching observed in air-annealed samples [45, 63]. Thermogravimetric analysis (TGA) conducted in air and N_2 atmosphere also indicates changes in the OLA decomposition process [64]. In fact, for the CQDs measured in air, we observe an initial weight loss of 7.36% at around 338°C, which is attributed to the decomposition of OLA ligands [45]. This was followed by further weight loss of 4.16% at 462°C. In contrast, the sample analyzed in nitrogen atmosphere exhibited initial weight loss of 15.66% at higher temperature (at around 400°C) due to the absence of oxidative environment (see Figure S17a,b).

The temperature can significantly influence the work function of semiconductor materials, particularly in CQDs, which are capped with surface ligands [45, 65]. To investigate this effect on InAs/ZnSe CQD thin films capped with OLA ligands, we performed Kelvin Probe Force Microscopy (KPFM) measurements. The obtained contact potential difference (CPD) [66, 67] maps quantify the difference in work function between the sample (in this case, InAs/ZnSe CQDs) and the conductive probe tip [67]:

$$CPD = (\Phi p - \Phi s) / |e| \quad (1)$$

where Φ_p (~ 4.78 eV) and Φ_s are the work functions of the probe tip and sample, respectively, and e is the elementary charge. This approach allows for direct correlation between local surface potential variations and the electronic structure of the thin film, given that increases/decreases in CPD values correspond to declines/rises in the work function [68] (Equation 1). The surface morphology (scanned area for CPD) and corresponding CPD map of the InAs/ZnSe CQD thin film on SiO_2/Si substrate annealed at 250°C are shown in Figure 3a–c. The average CPD profile (taken from 12 scan lines) is presented in Figure 3c, and the corresponding average CPD values are indicated in Figure 3d.

Data for RT, 200°C, and 300°C is provided in Figure S18a–i, where further degradation of the film is clearly visible for the latter, consistent with Raman and XPS analyses. A pronounced increase in CPD is observed up to 250°C (Figure 3d), reaching a maximum of ~1.1 V. This enhancement in CPD can be attributed to the partial removal of organic ligands, which enhances electronic coupling between neighboring CQDs. These changes effectively shift the Fermi level, leading to a higher surface potential. Since InAs/ZnSe CQDs are n-type in nature, we attribute the significant CPD changes observed at 250°C primarily to a change in work function, rather than contributions from trapped charges or dipoles [45, 69]. However, upon further annealing to 300°C, the CPD decreases sharply, consistent with the degradation observed in the AFM analysis (Figures S6 and S18g) and in the XPS analysis, where the InAs/ZnSe CQDs form oxides (Figure 2g). At this stage, the extensive removal of ligands and coalescence of CQDs likely disrupt the uniformity of the film, generating a variety of different defects. These results highlight that annealing at 250°C provides an optimum balance between ligands removal and structural integrity, while higher annealing temperatures induce degradation of the CQDs thin film. [60, 36] To further support this claim, we first examined the Raman spectra of pure OLA, as shown in Figure S19a. At room temperature, the spectra exhibits a strong vibrational band in the 2800–3000 cm^{-1} region, corresponding to the C—H stretching modes, along with additional smaller molecular peaks, including D (~1320 cm^{-1}) and G (~1580 cm^{-1}) modes from carbon, characteristic of OLA [45, 66]. After annealing at 250°C, these well-defined C-H bands disappear, leaving only the silicon substrate peak (Figure S19a, purple curve) accompanied by a dominant fluorescent background. The absence of the D and G bands further suggests that the annealed residue is either highly disordered or amorphous carbon, rather than graphitic domains [45, 66]. A similar trend is observed in the InAs/ZnSe CQD film annealed at 250°C (Figure S19b). The spectrum reveals a pronounced longitudinal optical (LO) phonon mode near 250 cm^{-1}, confirming the retention of the crystalline structure. However, the C-H stretching vibrations are no longer detected, consistent with the decomposition of OLA ligands. The spectra are dominated instead by a broad background, caused by luminescence from the CQDs (Figure S19b,) [45]. The ligand removal reduces the distance among CQDs, promoting improved interconnectivity within the film. This improved connectivity is reflected in the decreased work function measured by KPFM, suggesting a correlation between ligand decomposition, structural rearrangement, and enhanced electronic properties [38].

The insight provided by KPFM motivated us to investigate the current density-voltage (J-V) characteristics of CQD films annealed at different temperatures. To study the *J-V* characteristics we fabricated devices as schematically illustrated in Figure 4a.

The optical picture of the device annealed at 250°C is reported in Figure 4b where S and D are marked on the Au pad indicating the drain and source electrodes, their corresponding SEM image is also shown. The inset (below) of Figure 4b presents a higher magnification SEM image of the InAs/ZnSe CQD film, demonstrating the active material in the electrical channel.

The *J-V* characteristics of the InAs/ZnSe CQD thin-film under ambient conditions are reported in Figure 4c. The pristine film (Figure 4c, black curve) exhibits no electrical conduction, which is expected due to the presence of long-chain OLA ligands that hinder charge transport. At 200 °C, a similar *J-V* curve is observed with a lack of electrical conductivity; yet we observed a small and gradual change in the work function (Figure 3d). Interestingly, at 250°C (Figure 4c purple curve), the current density (J) increases dramatically, and a distinct non-linear *J-V* characteristic emerges. Upon further heating (300°C), the current density decreases, as

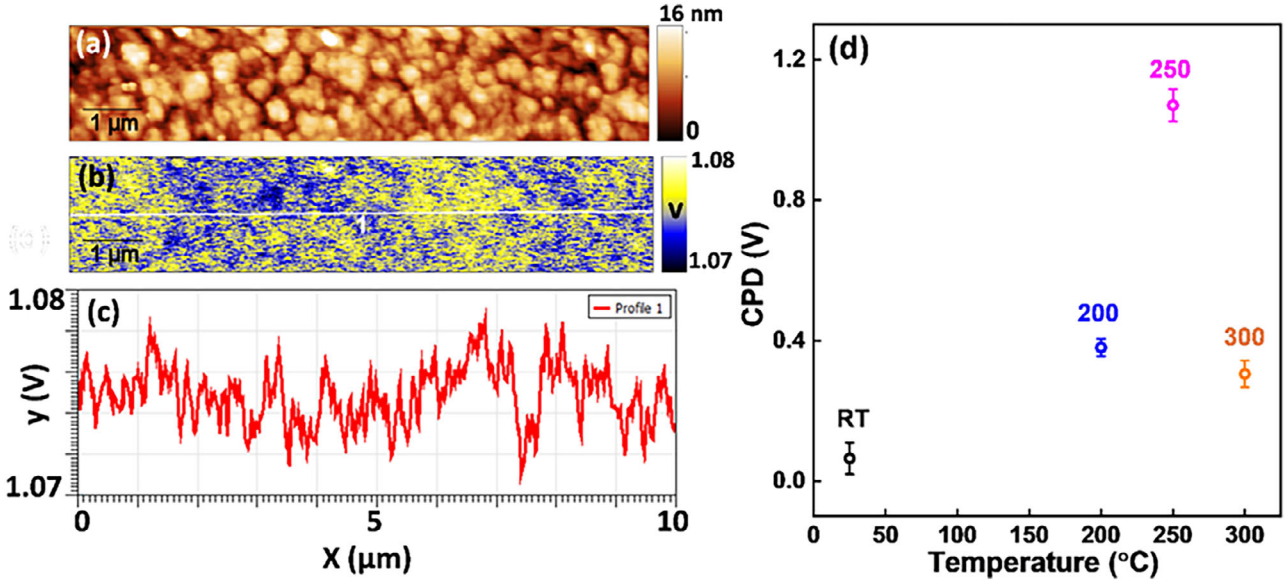

FIGURE 3 | (a) AFM image of InAs/ZnSe CQD thin films annealed at 250°C. (b) Corresponding contact potential difference (CPD) map acquired simultaneously over the same scan areas. The white line in (b) indicates the path along which the CPD values were calculated, shown as CPD voltage versus probe position in (c). (c) CPD voltage versus probe position of InAs/ZnSe CQD thin film. (d) CPD voltage as a function of annealing temperature for the InAs/ZnSe CQD thin film.

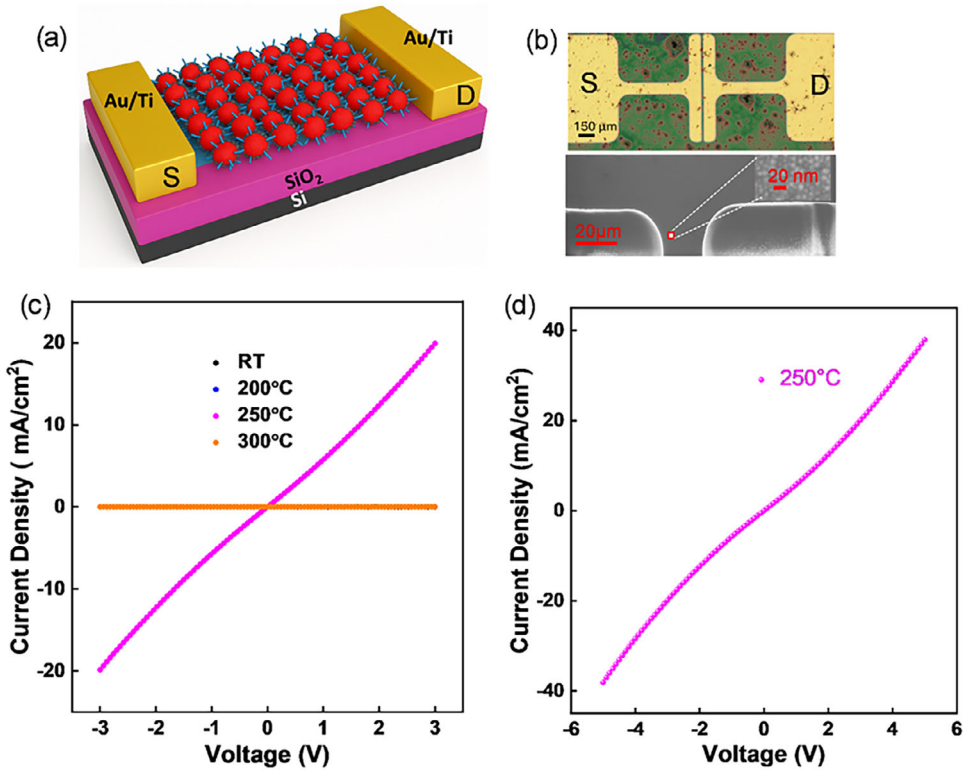

FIGURE 4 | (a) Schematic illustration of the fabricated device on a SiO_2/Si substrate, where Au serves as the source and drain electrodes, Ti as an adhesion layer, and InAs/ZnSe CQDs act as the active channel material. (b) Optical microscope and SEM images of the fabricated device annealed at 250°C, showing electrodes and CQD coverage between electrodes (inset under high resolution). (c) Current density-voltage (*J-V*) characteristics of devices annealed at different temperatures (RT, 200°C, 250°C, and 300°C). (d) Extended *J-V* measurement of the 250°C annealed device, demonstrating stable and symmetric current response over a wider voltage range (−5 V to 5 V).

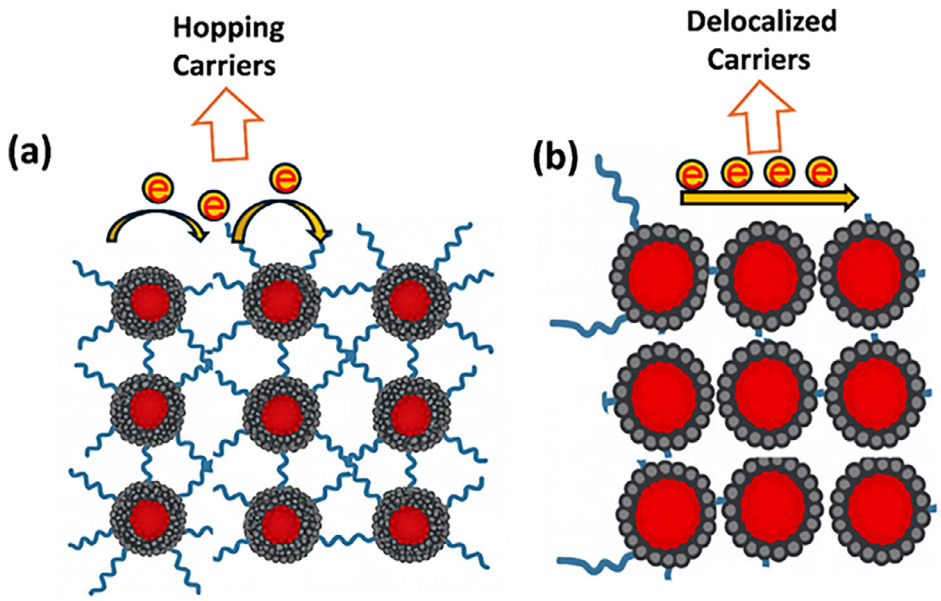

FIGURE 5 | Schematic illustration of the temperature-dependent charge transport mechanism in InAs/ZnSe CQD thin films. (a) Up to 200°C the CQDs are spatially separated by long-chain OLA ligands (blue wavy lines), limiting charge carrier transport to the thermally activated hopping mechanism. (b) At 250°C, further ligand removal results in reduced inter-CQD spacing, promoting charge delocalization and facilitating electrical transport.

expected, given the degradation of the CQD thin film. The *J-V* curves are also plotted separately in Figure S20a–c. To evaluate device robustness, we measured the *J-V* characteristics under an extended voltage range of −5 to 5 V for the 250°C sample. The device consistently maintains its symmetric non-linear Schottky behavior, demonstrating excellent electrical stability as shown in Figure 4d.

Additionally, we conducted *J-V* measurements of InAs/ZnSe CQD films annealed in N_2 and air [45]. Figure S21 shows the J-V curves for the two different annealing environments, where an increase in current density for the sample annealed in N_2 with respect to air is observed [45].

It is important to consider that InAs/ZnSe CQDs are capped with OLA ligands, which provide colloidal stability through their long alkyl chains and amine (-NH_2) functional group. However, these organic ligands act as insulating barriers between adjacent CQDs, significantly hindering charge transport. Consequently, InAs/ZnSe CQDs exhibit high electrical resistance, as reported in prior studies [33]. Based on our *J-V* measurements, we can rationalize the improvement in electrical conductivity upon annealing as follows (Figure 5): at room temperature (RT), the CQDs are stabilized by long-chain OLA ligands forming substantial insulating barriers between neighboring quantum dots (Figure 5a). These ligands impede charge carrier transport, resulting in very high electrical resistance and negligible current density, consistent with the behavior observed in Figure 4c.

At 200°C, partial desorption of the OLA ligands occurs, reducing the interparticle distance and promoting closer packing of the CQDs. Nonetheless, conduction remains negligible. At 250°C, further reduction in interparticle spacing takes place, leading to a more compact and interconnected CQD network (Figure 5b). The insulating gaps between CQDs are reduced, allowing a transition from hopping-dominated charge transport to another one characterized by increased charge delocalization across neighboring CQDs. Consequently, band-like or percolative transport mechanisms become more prominent. This annealing temperature represents an optimal balance between ligand removal and preservation of CQD order, resulting in an enhancement in carrier mobility and electrical conductivity. These observations align well with recent work by Chang et al., who reported that OLA ligands begin desorbing above 200°C under open atmosphere annealing conditions [45]. Further increasing the temperature to 300°C results in a decrease in current density (Figure S20), due to the degradation of the CQDs and formation of oxides.

3 | Conclusion

We have systematically investigated the temperature-dependent optical, structural, and electrical properties of InAs/ZnSe CQDs by annealing the films in ambient atmosphere up to 300°C. The optical characterization reveals that the PL and carrier lifetime are partially maintained up to 250°C. Complementary Raman spectroscopy and XRD confirm that the crystalline structure of the CQDs is maintained up to 300°C, with no observable phase degradation, demonstrating their robust structural integrity under thermal treatment. KPFM data reveals a pronounced and an abrupt change in the work function at 250°C. The CQD films exhibit insulating characteristics up to 200°C, consistent with the presence of intact OLA ligands acting as insulating barriers. Above 200°C, partial ligand desorption occurs, allowing the CQDs to pack closer together and enabling enhanced charge carrier delocalization. This leads to a dramatic increase in current density and electrical conductivity at 250°C. Our study provides fundamental insights into the thermally induced evolution of InAs/ZnSe CQD films, offering a straightforward and effective route to tune their optoelectronic properties

through thermal annealing. Notably, annealing under inert N_2 atmosphere preserves higher PL intensity compared to annealing in air, confirming that controlled environments enable further optimization of optical as well as electrical performance by minimizing surface oxidation effects while maintaining structural integrity.

4 | Experimental Details

4.1 | Materials

Indium (III) chloride ($InCl_3$, 99.99%), Zinc (II) chloride ($ZnCl_2$, 99.99%), alane *N,N*-dimethylethylamine complex solution (DMEA-AlH_3, 0.5 M solution in toluene), and oleylamine (OLA, 98%) were purchased from Sigma-Aldrich. Tri-n-octylphosphine (TOP, 97%), Selenium powder (Se, 99.99%), and Tris(dimethylamino) arsine (amino-As, 99%) were purchased from Strem Chemicals. Toluene (anhydrous, 99.8%) and ethanol (anhydrous, 99.8%) were purchased from Sigma-Aldrich. All chemicals were used without further purification.

4.2 | Preparation of Precursors

4.2.1 | Preparation of Amino-As precursor

In a glovebox, 0.2 mmol amino-As was added to 0.5 mL of degassed OLA and mixed for 5 min at 40°C until no bubbles further evolved.

4.2.2 | Preparation of $ZnCl_2$-OLA (0.8 M) Precursor

In a glovebox, 8 mmol $ZnCl_2$ was mixed with 10 mL of degassed OLA at 250°C for 1 h. Due to its solidification at room temperature, it is required to preheat before injection.

4.2.3 | Preparation of TOP-Se (1 M) Precursor

To prepare a stock TOP-Se solution, 10 mmol of powder selenium was mixed with 10 mL of trioctylphosphine (TOP) under constant stirring at 130°C for 15 min. Then, it was cooled down to room temperature and was kept in glovebox for further experiments.

4.3 | Core and Core-Shell Quantum Dot Synthesis

InAs core and InAs/ZnSe core-shell QDs were synthesized through a modified literature method [29], using amino-As as precursor. First, to synthesize InAs core, a mixture of 0.2 mmol $InCl_3$, 4 mmol of $ZnCl_2$, and 5 mL of OLA was degassed at 120°C for 1 h and then heated to 240°C under an inert atmosphere. Upon reaching 240°C, amino-As and 1.2 mL DMEA-AlH_3 were quickly injected into the main solution and mixed at 300°C for 15 min. Afterward, it cooled down to room temperature. For the precipitation, toluene and ethanol were used and it was centrifuged at 6000 rpm for 3 min. For InAs/ZnSe core-shell QDs, instead of cooling down to RT, the crude solution was cooled to 90°C. Subsequently, 2,5 mL $ZnCl_2$-OLA and 7,5 mL TOP-Se solutions were injected, and the temperature was raised to 310°C. At that temperature, the crude solution was mixed for 2 h and cooled down to RT. The resulting QDs were precipitated using toluene and ethanol at 6000 rpm 3 min. The purification step was repeated 3 times. The final products, including core and core-shell QDs, were dissolved in anhydrous toluene.

4.4 | Optical Characterization

Optical absorption spectra were recorded on a Varian Cary 5000 UV–vis-NIR spectrophotometer. For PL, measurements were conducted using an Edinburgh Instruments FLS900 fluorescence spectrometer equipped with an Xe lamp. A Renishaw Raman system was utilized to collect high-resolution Raman spectroscopy and micro-PL data. The Raman measurements were carried out using an 1800 grating, with a 633 nm excitation wavelength and a power of 0.5 mW, employing a 100X objective lens under ambient conditions. Micro PL was measured using 514 nm excitation using a 600 grating at 0.3 mW. Zeta Profilometer was used to capture optical pictures of the films.

4.5 | Structural Characterization

4.5.1 | Transmission Electron Microscopy (TEM)

TEM measurements were conducted using a JEOL JEM-1400Plus microscope with a thermionic gun (W filament) operated at an acceleration voltage of 120 kV. Atomic resolution scanning STEM images were acquired on a probe-corrected Thermo Fisher Spectra 30–300 S/TEM operated at 300 kV. High resolution images were acquired on a high-angle annular dark field (HAADF) detector with a current of 40 pA and a beam convergence semi angle of 25 mrad. Compositional maps were acquired using Velox, with a probe current of ∼150 pA and rapid rastered scanning by the Energy-Dispersive X-Ray (EDX) spectroscopy on a Dual-X setup comprising two detectors on either side of the sample, for a total acquisition solid angle of 1.76 Sr.

The high-resolution surface morphology was acquired using a Zeiss Gemini SEM560 field-emission scanning electron microscope (FE-SEM). Elemental analysis and mapping were performed by EDX with an 80 mm^2 SDD detector (Oxford XMax-80).

4.5.2 | X-Ray Diffraction

XRD spectra of the films were collected using the PANanalytical Empyrean X-ray diffractometer equipped with a 1.8 kW Cu Kα ceramic X-ray tube and a PIXcel3D 2×2 area detector, operating at 40 mA and 45 kV using parallel beam geometry and symmetric reflection mode. The InAs/ZnSe CQDs were deposited on a quartz substrate. XRD patterns were acquired at room temperature under ambient conditions.

4.5.3 | Atomic Force Microscopy

AFM analysis was performed with a Veeco Multimode /Nanoscope IV system in tapping mode to obtain thickness and surface morphology of the InAs/ZnSe CQD film. Data processing was carried out with Gwyddion.

4.5.4 | X-Ray Photoelectron Spectroscopy (XPS)

XPS measurements were performed with a Kratos Axis UltraDLD spectrometer, using a monochromatic Al Kα source operated at 20 mA and 15 kV. High resolution analyses were carried out with an analysis area of 300 × 700 microns and a pass energy of 20 eV. The Kratos charge neutralizer system was used on all specimens. Spectra have been charge corrected to the main line of the carbon 1s spectrum (adventitious carbon) set to 284.8 eV. Spectra were analyzed using CasaXPS software (version 2.3.24) [70].

Thermogravimetric Analysis (TGA): Thermal gravimetric analysis (TGA) was conducted with a TA Instruments Q500 thermal analyzer under a 50 mL/min nitrogen flux on ~5 mg of nanocrystals powders. After a 5 min equilibration at 30°C, the samples were heated to 700°C, at rate of 10°C/min.

4.6 | Electrical Characterization

4.6.1 | Device Fabrication

For device fabrication, a shadow mask (purchased from Ossila) was employed to define the electrode geometry on the InAs/ZnSe CQDs film deposited on a SiO_2/Si thin film substrate. Subsequently, Au (5 nm) and Ti (80 nm) electrodes were deposited sequentially using an electron-beam evaporator, ensuring clean interfaces and well-controlled film thicknesses. A detailed description of the InAs/ZnSe CQDs thin-film preparation procedure, along with step-by-step instructions, is provided in Figure S4 of the Supporting Information.

4.6.2 | Kelvin Probe Force Microscopy

KPFM measurements were performed using an Asylum Research MFP-3D system enclosed within a nitrogen glovebox, where the relative humidity was maintained below 20% to ensure environmental stability. Bruker SCM-PIT-V2 cantilevers were employed, exhibiting a typical resonance frequency of 70–75 kHz, a spring constant of approximately 3 N/m, a tip radius of 25 nm, and a tip height ranging from 10 to 15 µm. Both the tip cone and cantilever were coated with a PtIr alloy (work function ≈ 4.78 eV). Topography acquisition was conducted in amplitude modulation (AM) mode on the first eigenmode, with the oscillation amplitude set between 20 and 40 nm. KPFM was implemented using the dual-pass "NAP" mode provided by the Asylum system. In the first pass, surface topography was mapped in tapping mode. During the second pass, the cantilever was lifted to a fixed height of 50 nm, its mechanical drive disabled, and an AC voltage was applied at the cantilever's resonance frequency. To nullify the tip-sample electrostatic interaction, a compensating DC voltage (V_{DC}) was applied. The resulting V_{DC} values were recorded pointwise to construct spatially resolved maps of the contact potential difference (V_{CPD}). Assuming that tip and sample form a parallel plate capacitor at any given time during the second pass (topographic contribution is minimized):

$$V_{CPD} = (\Phi s - \Phi p)/e \quad (2)$$

where e is the positive elementary charge and Φ_s and Φ_p are the sample (s) and probe (p) work functions, respectively. The sample work function (Φ_s) is calculated after an estimation/calibration of the tip work function (Φ_p, different tips have different work functions). Each tip is therefore calibrated by acquiring a scan on a freshly cleaved HOPG surface.

4.6.3 | J-V Characteristics Measurement

The electrical characterization (I-V) of the InAs/ZnSe CQDs device was conducted using a Suss MicroTec probe station equipped with an Olympus microscope. DC voltage and current measurements were performed using a Keithley 2614B source meter under normal conditions at room temperature.

Acknowledgements

We acknowledge support from the European Union's Horizon Europe research and innovation program through the following projects: Marie Sklodowska-Curie postdoctoral fellowship INFRALIGHT (101152448), European Innovation Council Pathfinder Challenges project RADIANT (101162112) and Pathfinder Open project LEAF (101186701), and the European Research Council proof-of-concept project MOONSHOT (101156586) and Starting Grant project Light-DYNAMO (850575). Part of this work was performed in the Clean Room Facility of the Istituto Italiano di Tecnologia; its support and resources are acknowledged. The authors acknowledge Giammarino Pugliese for the support in TGA analysis. Finally, we thank Simone Lauciello for support in collecting the SEM images and compositional maps.

Open access publishing facilitated by Istituto Italiano di Tecnologia, as part of the Wiley - CRUI-CARE agreement.

Conflicts of Interest

The authors declare no conflicts of interest.

Data Availability Statement

The data that support the findings of this study are available from the corresponding author upon reasonable request.

References

1. J. Shamsi, A. S. Urban, M. Imran, L. De Trizio, and L. Manna, "Metal Halide Perovskite Nanocrystals: Synthesis, Post-synthesis Modifications, and Their Optical Properties," *Chemical Reviews* 119 (2019): 3296–3348, https://doi.org/10.1021/acs.chemrev.8b00644.

2. L. Manna, D. J. Milliron, A. Meisel, E. C. Scher, and A. P. Alivisatos, "Controlled Growth of Tetrapod-branched Inorganic Nanocrystals," *Nature Materials* 2 (2003): 382–385, https://doi.org/10.1038/nmat902.

3. X. Peng, L. Manna, W. Yang, et al., "Shape Control of CdSe Nanocrystals," *Nature* 404 (2000): 59–61, https://doi.org/10.1038/35003535.

4. K. C. Dümbgen, R. Pascazio, B. van Beek, Z. Hens, and I. Infante, "Classical Force Field Parameters for InP and InAs Quantum Dots With Various Surface Passivations," *Journal of Physical Chemistry A* 127 (2023): 3427.

5. Q. A. Akkerman, M. Gandini, F. Di Stasio, et al., "Strongly Emissive Perovskite Nanocrystal Inks for High-voltage Solar Cells," *Nature Energy* 2 (2016): 16194, https://doi.org/10.1038/nenergy.2016.194.

6. X. Xue, M. Chen, Y. Luo, T. Qin, X. Tang, and Q. Hao, "High-operating-temperature Mid-infrared Photodetectors via Quantum Dot Gradient Homojunction," *Light: Science & Applications* 12 (2023): 2, https://doi.org/10.1038/s41377-022-01014-0.

7. D. Hahm, V. Pinchetti, C. Livache, et al., "Colloidal Quantum Dots Enable Tunable Liquid-state Lasers," *Nature Materials* 24 (2025): 48–55, https://doi.org/10.1038/s41563-024-02048-y.

8. A. R. C. Osypiw, S. Lee, S.-M. Jung, et al., "Solution-Processed Colloidal Quantum Dots for Light Emission," *Material Advance* 3 (2022): 6773.

9. H. M. Gil, T. W. Price, K. Chelani, J.-S. G. Bouillard, S. D. J. Calaminus, and G. J. Stasiuk, "NIR-quantum Dots in Biomedical Imaging and Their Future," *iScience* 24 (2021): 102189.

10. Z. U. Khan, L. U. Khan, H. F. Brito, M. Gidlund, O. L. Malta, and P. Di Mascio, "Colloidal Quantum Dots as an Emerging Vast Platform and Versatile Sensitizer for Singlet Molecular Oxygen Generation," *ACS Omega* 8 (2023): 34328–34353, https://doi.org/10.1021/acsomega.3c03962.

11. H. Lin, C. Wang, J. Wu, Z. Xu, Y. Huang, and C. Zhang, "Colloidal Synthesis of MoS2 Quantum Dots: Size-dependent Tunable Photoluminescence and Bioimaging," *New Journal of Chemistry* 39 (2015): 8492–8497, https://doi.org/10.1039/C5NJ01698C.

12. M. K. Thakur, A. Asaithambi, L. Rebecchi, S. Kuriyil, and I. Kriegel, *Emerging Materials for Energy and Sensing Applications* (CRS, Press, 2025): 80.

13. A. Gupta, S. Ghosh, M. K. Thakur, et al., "Up-conversion Hybrid Nanomaterials for Light-and Heat-driven Applications," *Progress in Materials Science* 121 (2021): 100838, https://doi.org/10.1016/j.pmatsci.2021.100838.

14. M. K. Thakur, A. Gupta, M. Y. Fakhri, et al., "Optically Coupled Engineered Upconversion Nanoparticles and Graphene for a High Responsivity Broadband Photodetector," *Nanoscale* 11 (2019): 9716–9725, https://doi.org/10.1039/C8NR10280E.

15. A. Gupta, M. K. Thakur, T. A. Effendi, et al., "Metallo-graphene Enhanced Upconversion Luminescence for Broadband Photodetection Under Polychromatic Illumination," *Chemical Engineering Journal* 420 (2021): 127608, https://doi.org/10.1016/j.cej.2020.127608.

16. M. K. Thakur, C.-Y. Fang, Y.-T. Yang, et al., "Microplasma-enabled Graphene Quantum Dot-wrapped Gold Nanoparticles With Synergistic Enhancement for Broad Band Photodetection," *ACS Applied Materials & Interfaces* 12 (2020): 28550–28560, https://doi.org/10.1021/acsami.0c06753.

17. A. Asaithambi, M. K. Thakur, D. Zhu, et al., "Charge Transfer in InAs@ZnSe-MoS 2 Heterostructures for Broadband Photodetection," *Advanced Functional Materials* 34 (2024): 2409951, https://doi.org/10.1002/adfm.202409951.

18. M. Pegu, H. Roshan, C. Otero-Martínez, et al., "Improving the Stability of Colloidal CsPbBr3 Nanocrystals With an Alkylphosphonium Bromide as Surface Ligand Pair," *ACS Energy Letters* 10 (2025): 2268–2276, https://doi.org/10.1021/acsenergylett.5c00124.

19. H. Saleem, A. Saud, and S. J. Zaidi, "Sustainable Preparation of Graphene Quantum Dots From Leaves of Date Palm Tree," *ACS Omega* 8 (2023): 28098–28108, https://doi.org/10.1021/acsomega.3c00694.

20. S. Iravani and R. S. Varma, "Green Synthesis, Biomedical and Biotechnological Applications of Carbon and Graphene Quantum Dots. A Review," *Environmental Chemistry Letters* 18 (2020): 703–727, https://doi.org/10.1007/s10311-020-00984-0.

21. L. Meng, Q. Xu, J. Zhang, and X. Wang, "Colloidal Quantum Dot Materials for next-generation near-infrared Optoelectronics," *Chemical Communications* 60 (2024): 1072–1088, https://doi.org/10.1039/D3CC04315K.

22. M. Chen, H. Lu, N. M. Abdelazim, et al., "Mercury Telluride Quantum Dot Based Phototransistor Enabling High-sensitivity Room-temperature Photodetection at 2000 Nm," *ACS Nano* 11 (2017): 5614–5622, https://doi.org/10.1021/acsnano.7b00972.

23. H. Roshan, D. Zhu, D. Piccinotti, et al., "Near Infrared Light-Emitting Diodes Based on Colloidal InAs/ZnSe Core/Thick-Shell Quantum Dots," *Advanced Science* 11 (2024): 2400734.

24. M. De Franco, D. Zhu, A. Asaithambi, et al., "Near-infrared Light-emitting Diodes Based on RoHS-compliant InAs/ZnSe Colloidal Quantum Dots," *ACS Energy Letters* 7 (2022): 3788–3790, https://doi.org/10.1021/acsenergylett.2c02070.

25. D. Zhu, F. Bellato, H. Bahmani Jalali, et al., "ZnCl2 Mediated Synthesis of InAs Nanocrystals With Aminoarsine," *Journal of the American Chemical Society* 144 (2022): 10515–10523, https://doi.org/10.1021/jacs.2c02994.

26. R. Xie, K. Chen, X. Chen, and X. Peng, "InAs/InP/ZnSe Core/Shell/Shell Quantum Dots as near-infrared Emitters: Bright, Narrow-band, Non-cadmium Containing, and Biocompatible," *Nano Research* 1 (2008): 457–464, https://doi.org/10.1007/s12274-008-8048-x.

27. S. Kim, S. Yeon, M. Lee, et al., "Chemically and Electronically Active Metal Ions on InAs Quantum Dots for Infrared Detectors," *NPG Asia Materials* 15 (2023): 30, https://doi.org/10.1038/s41427-023-00477-w.

28. M.-J. Si, S. Jee, M. Yang, et al., "Colloidal InAs Quantum Dot-Based Infrared," *Advanced Science* 11 (2024): 2306798.

29. D. Zhu, H. Bahmani Jalali, G. Saleh, et al., "Boosting the Photoluminescence Efficiency of InAs Nanocrystals Synthesized With Aminoarsine via a ZnSe Thick-Shell Overgrowth," *Advanced Materials* 35 (2023): 2303621, https://doi.org/10.1002/adma.202303621.

30. S. Panda, D. Zhu, L. Goldoni, et al., "Overcoming the Short-Wave Infrared Barrier in the Photoluminescence of Amino-As-Based InAs Quantum Dots," *Advanced Optical Materials* 13 (2025): 01512, https://doi.org/10.1002/adom.202501512.

31. H. B. Jalali, L. De Trizio, L. Manna, and F. Di Stasio, "Indium Arsenide Quantum Dots: An Alternative to Lead-based Infrared Emitting Nanomaterials," *Chemical Society Reviews* 51 (2022): 9861–9881, https://doi.org/10.1039/D2CS00490A.

32. C. Hu, A. I. Channa, L. Xia, et al., "Colloidal InAs Quantum Dots: Synthesis, Properties, and Optoelectronic Devices," *Advance Functional Materials* 35 (2025): 2500280.

33. B. Li, Y. Wang, J. Zhang, et al., "Efficient and Stable near-infrared InAs Quantum Dot Light-emitting Diodes," *Nature Communications* 16 (2025): 2450, https://doi.org/10.1038/s41467-025-57746-1.

34. J. Leemans, V. Pejović, E. Georgitzikis, et al., "Colloidal III–V Quantum Dot Photodiodes for Short-Wave Infrared Photodetection," *Advanced Science* 9 (2022): 2200844, https://doi.org/10.1002/advs.202200844.

35. P. Xia, B. Sun, M. Biondi, et al., "Sequential Co-Passivation in InAs Colloidal Quantum Dot Solids Enables Efficient Near-Infrared Photodetectors," *Advanced Materials* 35 (2023): 2301842, https://doi.org/10.1002/adma.202301842.

36. T. Sheikh, W. J. Mir, A. Alofi, et al., "Surface-reconstructed InAs Colloidal Nanorod Quantum Dots for Efficient Deep-shortwave Infrared Emission and Photodetection," *Journal of the American Chemical Society* 146 (2024): 29094–29103, https://doi.org/10.1021/jacs.4c10755.

37. Y. Park, J. Kim, M. Jeong, et al., "Pb-Free Infrared Harvesting Colloidal Quantum Dot Solar Cells Using n-p Homojunction Architecture," *Advance Energy Mater* 2025, 15, 2404141.

38. J. Seo, S. Kim, D. Yeo, N. Gwak, and N. Oh, "Pnictide-based Colloidal Quantum Dots for Infrared Sensing Applications," *Nano Convergence* 12 (2025): 26, https://doi.org/10.1186/s40580-025-00489-y.

39. M. Liu, G. Tang, Y. Liu, and F.-L. Jiang, "Ligand Exchange of Quantum Dots: A Thermodynamic Perspective," *Journal of Physical Chemistry Letters* 15 (2024): 1975.

40. H. W. Ban, M. Vafaie, L. Levina, et al., "Resurfacing of InAs Colloidal Quantum Dots Equalizes Photodetector Performance Across Synthetic Routes," *Journal of the American Chemical Society* 146 (2024): 24935–24944, https://doi.org/10.1021/jacs.4c06202.

41. L. Asor, J. Liu, Y. Ossia, et al., "InAs nanocrystals with robust p-type doping," *Advance Functional Materials* 31 (2021): 2007456.

42. L. Asor, J. Liu, S. Xiang, N. Tessler, A. I. Frenkel, and U. Banin, "Zn-Doped P-Type InAs Nanocrystal Quantum Dots," *Advanced Materials* 35 (2023): 2208332.

43. J. Leemans, K. C. Dümbgen, M. M. Minjauw, et al., "Acid–Base Mediated Ligand Exchange on Near-Infrared Absorbing, Indium-Based

III–V Colloidal Quantum Dots," *Journal of the American Chemical Society* 143 (2021): 4290–4301, https://doi.org/10.1021/jacs.0c12871.

44. B. Sun, A. M. Najarian, L. K. Sagar, et al., "Fast Near-Infrared Photodetection Using III–V Colloidal Quantum Dots," *Advanced Materials* 34 (2022): 2203039.

45. K. Chang, C. Podder, and H. Pan, "Ligand Decomposition Differences During Thermal Sintering of Oleylamine-capped Gold Nanoparticles in Ambient and Inert Environments: Implications for Conductive Inks," *ACS Applied Nano Materials* 6 (2023): 23418–23429, https://doi.org/10.1021/acsanm.3c04803.

46. S. Bai, K. Haase, J. Perez Andrade, et al., "Impact of Thermal Annealing on the Dissolution of Semiconducting Polymer Thin Films," *Advanced Electronic Materials* 10 (2024): 2300801, https://doi.org/10.1002/aelm.202300801.

47. S. Ghosh, M. Abdelbaky, W. Mertin, E. Müller, and J. de Boor, "Surface Degradation of Mg2X-Based Composites at Room Temperature: Assessing Grain Boundary and Bulk Diffusion Using Atomic Force Microscopy and Scanning Electron Microscopy," *ACS Applied Materials & Interfaces* 16 (2024): 48619–48628, https://doi.org/10.1021/acsami.4c10236.

48. C. L. Chan, E. M. Sala, E. Clarke, and J. Heffernan, "Effects of Rapid Thermal Annealing on Telecom C-band InAs Quantum Dots on InP (100) Grown by Droplet Epitaxy," *Journal of Physics D: Applied Physics* 58 (2025): 025107, https://doi.org/10.1088/1361-6463/ad835d.

49. J. Chu, X. Liu, X. Zhang, et al., "Annealing Temperature Dependence of Mechanical and Structural Properties of Chromium-gold Films on the Silica Glass Substrate," *Thin Solid Films* 774 (2023): 139849, https://doi.org/10.1016/j.tsf.2023.139849.

50. I. du Fossé, S. Lal, A. N. Hossaini, I. Infante, and A. J. Houtepen, "Effect of Ligands and Solvents on the Stability of Electron Charged Cdse Colloidal Quantum Dots," *The Journal of Physical Chemistry C* 125 (2021): 23968–23975, https://doi.org/10.1021/acs.jpcc.1c07464.

51. R. Bose, G. Manna, and N. Pradhan, "Anisotropic Zinc Blende ZnSe Nanostructures: The Interface Chemistry and the Retention of Zinc Blende Phase During Growth," *The Journal of Physical Chemistry C* 117 (2013): 18762–18767, https://doi.org/10.1021/jp406358e.

52. Z. Liu, J. Llusar, H. H. Karakkal, et al., "Amino-Arsine and Amino-Phosphine Based Synthesis of InAs@ InP@ ZnSe Core@ Shell@ Shell Quantum Dots," *Advance Energy Mater* 2024, 14, 2402246.

53. Y. Zhao, K. Lu, J. Yao, et al., "Strain evolution and confinement effect in InAs/AlAs short-period superlattices studied by Raman spectroscopy," *Science Rep* 13 (2023): 123.

54. J. Xu, X. Yang, Q.-D. Yang, et al., "Arrays of CdSe Sensitized ZnO/ZnSe Nanocables for Efficient Solar Cells With High Open-circuit Voltage," *Journal of Materials Chemistry* 22 (2012): 13374, https://doi.org/10.1039/c2jm31970e.

55. M. Kamruzzaman and J. A. Zapien, "Synthesis and Characterization of ZnO/ZnSe NWs/PbS QDs Solar Cell," *Journal of Nanoparticle Research* 19 (2017): 125, https://doi.org/10.1007/s11051-016-3729-y.

56. P. Cavanaugh, I. Jen-La Plante, C. Ippen, R. Ma, D. F. Kelley, and A. M. Kelley, "Resonance Raman Study of Shell Morphology in InP/ZnSe/ZnS Core/Shell/Shell Nanocrystals," *The Journal of Physical Chemistry C* 125 (2021): 10549–10557, https://doi.org/10.1021/acs.jpcc.1c02616.

57. L. Borkovska, N. Korsunska, T. Stara, et al., "Effects of Bio-conjugation and Annealing on the Photoluminescence and Raman Spectra of CdSe/ZnS Quantum Dots," *MRS Proceedings* 1534 (2013): A113–A119, https://doi.org/10.1557/opl.2013.307.

58. Q. Cai, H. Zhou, and F. Lu, "The Effects of Thermal Annealing in Self-assembled Ge/Si Quantum Dots," *Applied Surface Science* 253 (2007): 4792–4795, https://doi.org/10.1016/j.apsusc.2006.10.045.

59. J. Langer, D. Jimenez de Aberasturi, J. Aizpurua, et al., "Present and Future of Surface-Enhanced Raman Scattering," *ACS Nano* 14 (2020): 28–117, https://doi.org/10.1021/acsnano.9b04224.

60. J. R. Shallenberger and N. Hellgren, "Zinc Selenide Analyzed by XPS," *Surface Science Spectra* 27 (2020): 014020, https://doi.org/10.1116/6.0000165.

61. N. Hellgren, M. A. Steves, J. Shallenberger, S. K. O'Boyle, E. Mellott, and A. R. Noble, "Effect of Etching on the Oxidation of Zinc Selenide Surfaces Characterized by X-ray Photoelectron Spectroscopy," *Applied Surface Science* 528 (2020): 146604, https://doi.org/10.1016/j.apsusc.2020.146604.

62. S. C. Ghosh, M. C. Biesinger, R. R. LaPierre, and P. Kruse, "X-ray Photoelectron Spectroscopic Study of the Formation of Catalytic Gold Nanoparticles on Ultraviolet-ozone Oxidized GaAs (100) Substrates," *Journal of Applied Physics* 101 (2007): 114322, https://doi.org/10.1063/1.2743729.

63. H. Baek, S. Kang, J. Heo, et al., "Insights Into Structural Defect Formation in Individual InP/ZnSe/ZnS Quantum Dots Under UV Oxidation," *Nature Communications* 15 (2024): 1671, https://doi.org/10.1038/s41467-024-45944-2.

64. M. S. Skorotetcky, W. J. Mir, T. Sheikh, et al., "Si-H Hydrosilane Reducing Agents for Size-and Shape-Controlled InAs Colloidal Quantum Dots," *Advanced Materials* 37 (2025): 2412105.

65. E. Moyen, A. Kanwat, S. Cho, H. Jun, R. Aad, and J. Jang, "Ligand Removal and Photo-activation of CsPbBr 3 Quantum Dots for Enhanced Optoelectronic Devices," *Nanoscale* 10 (2018): 8591–8599, https://doi.org/10.1039/C8NR01396A.

66. M. Bieletzki, T. Hynninen, T. M. Soini, et al., "Topography and Work Function Measurements of Thin MgO (001) Films on Ag (001) by nc-AFM and KPFM," *Physical Chemistry Chemical Physics* 12 (2010): 3203, https://doi.org/10.1039/b923296f.

67. M. K. Thakur, G. Haider, F. J. Sonia, et al., "Isotope engineered fluorinated single and bilayer graphene: Insights into fluorination selectivity, stability, and defect passivation," *Small* 19 (2023): 2205575.

68. H. Takehira, M. R. Karim, Y. Shudo, M. Fukuda, T. Mashimo, and S. Hayami, "Modulating the Work Function of Graphene by Pulsed Plasma Aided Controlled Chlorination," *Scientific Reports* 8 (2018): 17392, https://doi.org/10.1038/s41598-018-35668-x.

69. A. F. Abd Rahim, M. R. Hashim, N. K. Ali, M. Rusop, M. D. Johan Ooi, and M. Z. M. Yusoff, "Self-assembled Ge Islands and Nanocrystals by RF Magnetron Sputtering and Rapid Thermal Processing: The Role of Annealing Temperature," *Applied Surface Science* 275 (2013): 193–200, https://doi.org/10.1016/j.apsusc.2013.01.053.

70. N. Fairley, V. Fernandez, M. Richard-Plouet, et al., "Systematic and Collaborative Approach to Problem Solving Using X-ray Photoelectron Spectroscopy," *Applied Surface Science Advances* 5 (2021): 100112, https://doi.org/10.1016/j.apsadv.2021.100112.

Supporting Information

Additional supporting information can be found online in the Supporting Information section.

Supporting File: adom71040-sup-0001-SuppMat.pdf.